3D printed axisymmetric sound absorber with double porosity

T.G. Zieliński [1], **N. Dauchez** [2], **T. Boutin** [2], **F. Chevillotte** [3], **F-X. Bécot** [3], **R. Venegas** [4]
[1] Institute of Fundamental Technological Research, Polish Academy of Sciences,
ul. Pawińskiego 5B, 02-106 Warsaw, Poland
e-mail: **tzielins@ippt.pan.pl**

[2] Université de Technologie de Compiègne, Alliance Sorbonne Université, CNRS,
Laboratoire Roberval, Centre de recherche Royallieu,
CS 60319, 60203 Compiègne cedex, France

[3] MATELYS – Research Lab,
7 rue des Maraîchers (bâtiment B), F69120 Vaulx-en-Velin, France

[4] University Austral of Chile, Institute of Acoustics,
P.O. Box 567, Valdivia, Chile

Abstract
This paper shows that specific additive manufacturing (AM) technology can be used to produce double-porosity acoustic materials where main pore networks are designed and a useful type of microporosity is obtained as a side effect of the 3D printing process. Here, the designed main pore network is in the form of annular pores set around the axis of the cylindrical absorber. In this way, the axial symmetry of the problem is ensured if only plane wave propagation under normal incidence is considered, which allows for modelling with purely analytical expressions. Moreover, the outermost annular pore is bounded by the wall of the impedance tube used to measure the sound absorption of the material, so that experimental tests can be easily performed. Two different AM technologies and raw materials were used to fabricate axisymmetric absorbers of the same design, in one case obtaining a material with double porosity, which was confirmed by the results of multi-scale calculations validated with acoustic measurements.

1 Introduction

Modern AM technologies [1, 2, 3] have become extremely useful for prototyping and development of innovative materials, devices and engineering solutions in various fields of technology and science. Recently, inter-laboratory tests involving various AM technologies, raw materials and 3D printers have confirmed – albeit under certain conditions – the reproducibility of 3D printed sound absorbers with engineered pore networks [4]. In fact, in spite of many limitations (e.g. a relatively low resolution), these technologies are widely used in recent times to develop new acoustic materials [5, 6, 7, 8, 9, 10, 11, 12, 13, 14]. However, with rare exceptions [12], these can be treated as single-porosity solutions.

The aim of this paper is to demonstrate that a specific AM technology can be used to produce engineered acoustic materials with double porosity that significantly enhances their performance. The main idea is to use technology that provides a useful type of microporosity in the 3D printed structure. This usually undesirable side effect can be regarded as an advantage when combined with a suitable design of the main pores or slits to ensure beneficial high contrast of permeability between the two porosity scales, leading to the pressure diffusion phenomenon. In this way, an additional and very effective mechanism of acoustic wave energy dissipation is obtained, which can be engineered by adjusting the design of the main pore network. In this

work, this approach will be applied to a cylindrical sound absorber [15, 16] in which the main pore network is in the form of annular slits arranged around its axis and separating the core and the subsequent rings, which are 3D printed as microporous. Such a simple structure of the absorber can be easily manufactured and its axial symmetry allows for modelling with purely analytical expressions [15, 16], so that the entire design can be quickly optimised, in particular to engineer the pressure diffusion effect.

The outline of this paper is as follows. The design and manufacturing of axisymmetric sound absorbers with annular slits are discussed in Section 2. Section 3 provides all necessary formulae for modelling of such acoustic materials with single or double porosity. Sound absorption by axisymmetric absorbers is presented in Section 4, where the results of analytical calculations and numerical simulations are confronted with the acoustic measurements on 3D printed specimens. The main findings and conclusions are summarised in Section 5.

2 Design and additive manufacturing of axisymmetric absorbers

Figure 1 presents the design and 3D printed specimen of an axisymmetric absorber with annular slits, for which all multi-scale calculations can be done analytically [15, 16, 17]. Thanks to the axial symmetry, direct numerical simulations can also be easily performed using the two-dimensional finite element mesh shown in Figure 1(b). The absorber is in the form of a cylinder composed of three coaxial parts, viz. an elongated cylindrical core and two rings, all separated by annular slits, see Figures 1 and 2. Two specimens of the absorber were manufactured in substantially different AM technologies, viz.:

- Stereolithography (SLA) [2] – using *Formlabs Form 3B* device and a low-viscosity photopolymer resin as raw material, see Figure 1(c,d) for sample photos,

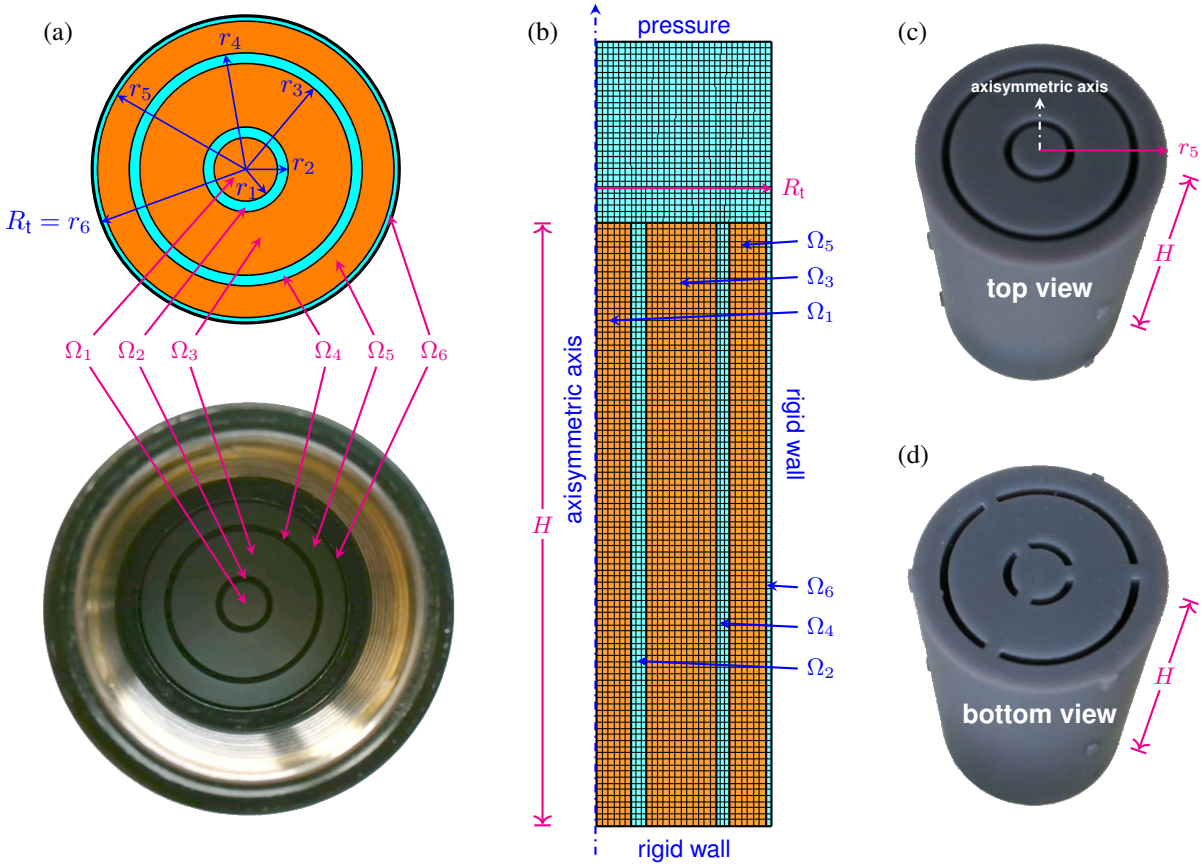

Figure 1: Axisymmetric absorbers with annular slits: (a) the geometry of the absorber inside the impedance tube, (b) finite element mesh used in numerical simulations, (c) top and (d) bottom view of the absorber specimen 3D printed from photopolymer resin in SLA technology.

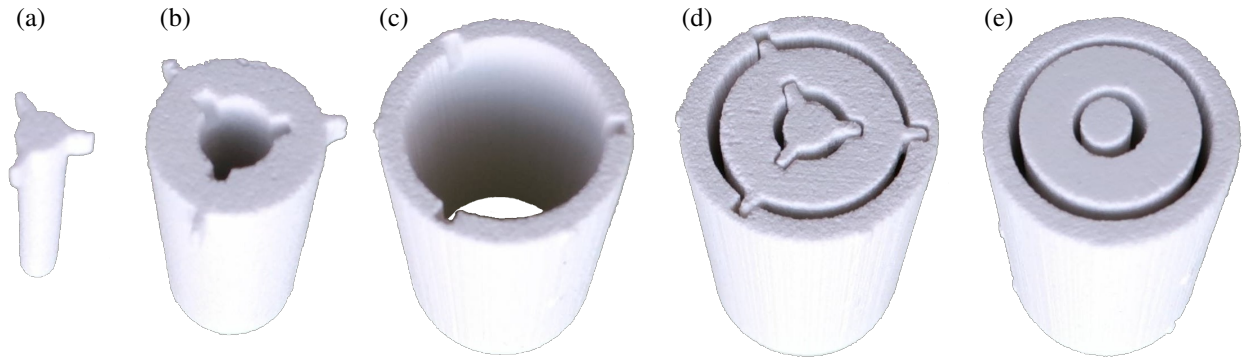

Figure 2: Axisymmetric absorber specimen 3D printed from gypsum powder in BJP technology: (a) cylindrical core, (b) inner ring, (c) outer ring, (d) bottom and (e) top view of the assembled sample.

- Binder Jetting 3D Printing (BJP) [3] – using *3D Systems ProJet 160* device and gypsum powder as raw material with butyrolactam as a binder, see Figure 2 for sample photos.

The SLA specimen was 3D printed as a single item, i.e. with all three parts already connected at the bottom as clearly seen in Figure 1(d), while the three parts of the BJP specimen were 3D printed separately and then assembled together, see Figure 2, due to the difficulty of removing the powder from the relatively narrow annular slits. As for the resin used in the SLA technology, its excess was easily removed from the slits due to its relatively low viscosity.

The main finding of this work – confirmed by the results discussed in Section 4 – is that the acoustic performance of the absorber strongly depends on the AM technology used to produce it. This is because the cylindrical core Ω_1 and two rings of the absorber, i.e. annular subdomains Ω_3 and Ω_5 (see Figure 1), are made of solid impervious material in the case of SLA technology, or microporous permeable material in the case of BJP technology. In each case, the absorber is installed in the impedance tube used for acoustic testing [18] as shown in the photo in Figure 1(a) for the SLA specimen. The tube radius is $R_\mathrm{t} = 14.5\,\mathrm{mm}$. In this configuration, there are three annular slits, Ω_2, Ω_4, and Ω_6, saturated with air. The wall of the external annular slit Ω_6 is formed by the internal surface of the metal tube. For practical reasons, the core and the two rings are connected by three small struts at the bottom of the absorber, although it is implemented differently in the SLA and BJP printouts, cf. Figures 1(d) and Figure 2(d). There are also six tiny bumps on the lateral surface of each absorber – three at the bottom and three in the middle of the height – which ensure the central positioning of the absorber in the tube. These small struts and bumps are 3D printed, but neglected in the modelling. Thus, all relevant dimensions of the absorber are defined by six radii r_n ($n = 1, \ldots, 6$) and the height $H = 50\,\mathrm{mm}$, as shown in Figure 1. Table 1 gives the nominal values of all radii and the corresponding annular widths from the geometric model used for 3D printing, as well as the actual values found by caliper measurements on 3D printed parts and microscope examination of annular slits, core and rings in 3D printed absorbers. The latter values differ slightly for SLA and BJP absorbers, as they depend on the additive manufacturing technology and the material used to make them. In addition, thorough examination of the 3D printed specimens confirmed the expected high quality of the SLA sample with very smooth surfaces and well-mapped shapes, as well as the lesser quality of the BJP sample with rough surfaces and shape distortions due to loose assembly. The actual dimensions listed in Table 1 were used to calculate

Table 1: Dimensions in axisymmetric absorbers with annular slits: (a) nominal values, (b) actual dimensions in the SLA absorber, (c) actual dimensions in the BJP absorber.

	Radii (mm)						Annular widths (mm)				
	r_1	r_2	r_3	r_4	r_5	$r_6 = R_\mathrm{t}$	$r_2 - r_1$	$r_3 - r_2$	$r_4 - r_3$	$r_5 - r_4$	$r_6 - r_5$
(a) nom.	3	4	10	11	14	14.5	1	6	1	3	0.5
(b) SLA	3.1	4.0	10.1	11.0	14.1	14.5	0.9	6.1	0.9	3.1	0.4
(c) BJP	2.9	4.1	9.9	11.0	14.0	14.5	1.2	5.8	1.1	3.0	0.5

the relevant macro-parameters during the multi-scale modelling of single- and double-porosity axisymmetric sound absorbers as discussed below.

3 Modelling based on analytical calculations

The acoustic wave propagation in porous materials with a rigid frame can be described by the classical Helmholtz equation for time-harmonic acoustics [19] that – in this case – results from the dynamic Darcy's law and macroscopic mass balance equation. The latter two equations are themselves derived by the homogenisation procedure involving the corresponding viscous flow and thermal diffusion problems formulated in the open pore network, and introducing two effective properties: the dynamic viscous permeability [20] and effective compressibility. The effective properties are complex-valued and depend on the angular frequency ω. The second one results from the so-called dynamic thermal permeability [21, 22] (related to the main pore network), and in the case of materials with double porosity it is also affected by the effective compressibility of air saturating the micropores, the effect of which can be greatly enhanced by the pressure diffusion phenomenon, described in modelling by the so-called dynamic pressure diffusion function [23, 24].

It has been demonstrated [24] that the aforementioned dynamic functions for viscous, thermal, and pressure diffusion effects, can be accurately calculated using the well-known scaling functions of the Johnson-Champoux-Allard-Lafarge-Pride (JCALP) model [19, 20, 21, 22, 25], provided that the relevant macro-parameters are known. In general, these parameters can be calculated by numerically solving the relevant boundary value problems (BVPs) formulated in the fluid domain (or microporous domain in the case related to pressure diffusion) of a periodic representative elementary volume [26, 27, 28, 24]. However, in the case of axisymmetric designs as the one studied in this work, all of these BVPs degenerate into the ordinary differential equation (see Appendix A.1), which can be solved analytically to provide closed formulae given in Appendix A, as demonstrated in [17] for the single-porosity case and in [15, 16] for the multi-scale absorber. In fact, all necessary formulae for analytical modelling of single- or double-porosity axisymmetric absorbers are provided below for the considered design with three annular slits, although a generalization can be readily made to any number of annular pores, see also Refs. [15, 16, 17].

As shown in Figure 1, the entire main pore network of each absorber consists of three annular slits, i.e. $\Omega_\mathrm{p} = \Omega_2 \cup \Omega_4 \cup \Omega_6$. Therefore, the porosity associated with this network is equal to the sum of the porosities of the individual slits, viz.

$$\phi_\mathrm{p} = \phi_\mathrm{p2} + \phi_\mathrm{p4} + \phi_\mathrm{p6}\,, \qquad \phi_\mathrm{p2} = \frac{r_2^2 - r_1^2}{R_\mathrm{t}^2}\,, \quad \phi_\mathrm{p4} = \frac{r_4^2 - r_3^2}{R_\mathrm{t}^2}\,, \quad \phi_\mathrm{p6} = \frac{r_6^2 - r_5^2}{R_\mathrm{t}^2}\,. \tag{1}$$

As demonstrated, e.g. in [17, 29], the static tortuosities, permeabilities and characteristic lengths of a pore network with all walls parallel to the direction of flow and wave propagation (as in the absorbers under consideration) are the same for viscous and thermal effects. Here, the static viscous $\mathcal{K}_\mathrm{0p}$ or thermal Θ_0p permeability is the sum of permeabilities calculated for each annular slit, viz.

$$\mathcal{K}_\mathrm{0p} = \Theta_\mathrm{0p} = \mathcal{K}_\mathrm{0p2} + \mathcal{K}_\mathrm{0p4} + \mathcal{K}_\mathrm{0p6}\,, \tag{2}$$

where (see Appendix A.3)

$$\mathcal{K}_\mathrm{0p2} = \Theta_\mathrm{0p2} = \frac{\phi_\mathrm{p2}\, r_2^2}{8}\left(1 + (r_1/r_2)^2 + \frac{1-(r_1/r_2)^2}{\ln(r_1/r_2)}\right), \tag{3}$$

$$\mathcal{K}_\mathrm{0p4} = \Theta_\mathrm{0p4} = \frac{\phi_\mathrm{p4}\, r_4^2}{8}\left(1 + (r_3/r_4)^2 + \frac{1-(r_3/r_4)^2}{\ln(r_3/r_4)}\right), \tag{4}$$

$$\mathcal{K}_\mathrm{0p6} = \Theta_\mathrm{0p6} = \frac{\phi_\mathrm{p6}\, r_6^2}{8}\left(1 + (r_5/r_6)^2 + \frac{1-(r_5/r_6)^2}{\ln(r_5/r_6)}\right). \tag{5}$$

The viscous and thermal characteristic lengths determined separately for each slit are equal to the width of

the respective slit, viz.

$$\Lambda_{\mathrm{vp}2} = \Lambda_{\mathrm{tp}2} = r_2 - r_1\,, \qquad \Lambda_{\mathrm{vp}4} = \Lambda_{\mathrm{tp}4} = r_4 - r_3\,, \qquad \Lambda_{\mathrm{vp}6} = \Lambda_{\mathrm{tp}6} = r_6 - r_5\,. \tag{6}$$

However, when determined for the entire network of slits, they are both equal to the half of the hydraulic diameter of that pore network, which means twice the ratio of the total cross sectional area of the annular pores to the corresponding total circumference, i.e.

$$\Lambda_{\mathrm{vp}} = \Lambda_{\mathrm{tp}} = \frac{r_6^2 - r_5^2 + r_4^2 - r_3^2 + r_2^2 - r_1^2}{r_6 + r_5 + r_4 + r_3 + r_2 + r_1}. \tag{7}$$

The slit walls are all parallel to the wave propagation direction so their network is not tortuous and the (kinematic) tortuosity $\alpha_{\infty\mathrm{p}} = 1$, because the end corrections can be neglected. Since the slit widths are comparable, the static (viscous and thermal) tortuosities calculated for each annular slit Ω_{n}, with $n = 2, 4, 6$, using the formula for α_0 derived in Appendix A.3, are almost identical and $\alpha_{0\mathrm{vp}n} = \alpha_{0\mathrm{tp}n} = 1.20$. However, the static tortuosity $\alpha_{0\mathrm{vp}} = \alpha_{0\mathrm{tp}}$ calculated for all the slits taken together is larger than this value (see Table 2).

Table 2: Macro-parameters and characteristic frequencies for viscous and thermal effects in the annular slits computed assuming: (a) nominal dimensions of the absorber design, (b) actual dimensions of the SLA absorber, (c) actual dimensions of the BJP absorber.

	ϕ_{p}	$\mathcal{K}_{0\mathrm{p}} = \Theta_{0\mathrm{p}}$	$\Lambda_{\mathrm{vp}} = \Lambda_{\mathrm{tp}}$	$\alpha_{0\mathrm{vp}} = \alpha_{0\mathrm{tp}}$	$\alpha_{\infty\mathrm{p}}$	f_{vp}	f_{tp}
	%	$10^{-8}\,\mathrm{m}^2$	mm	–	–	Hz	Hz
(a) nom.	20.10	1.252	0.748	1.482	1	40.1	56.7
(b) SLA	17.51	0.888	0.648	1.471	1	49.3	69.7
(c) BJP	21.71	1.724	0.809	1.507	1	31.3	44.2

Table 2 lists the values of all macro-parameters associated with the network of annular slits, calculated for the original design dimensions as well as the actual dimensions of the slits found in both 3D printed absorbers (see Table 1). These parameters, together with the formulae for shape factors

$$\mathcal{M}_{\mathrm{vp}} = \mathcal{M}_{\mathrm{tp}} = \frac{8\Theta_{0\mathrm{p}}}{\phi_{\mathrm{p}}\,\Lambda_{\mathrm{tp}}^2}\,, \qquad \mathcal{P}_{\mathrm{vp}} = \mathcal{P}_{\mathrm{tp}} = \frac{\mathcal{M}_{\mathrm{tp}}}{4\big(\alpha_{0\mathrm{tp}} - 1\big)}\,, \tag{8}$$

allow to calculate the corresponding dynamic viscous and thermal permeabilities, $\mathcal{K}_{\mathrm{p}}(\omega)$ and $\Theta_{\mathrm{p}}(\omega)$, using the following scaling functions [19, 20, 21, 22, 25]

$$\mathcal{K}_{\mathrm{p}}(\omega) = \mathcal{K}_{0\mathrm{p}} \left(\frac{\mathrm{i}\omega}{\omega_{\mathrm{vp}}} + 1 - \mathcal{P}_{\mathrm{vp}} + \sqrt{\mathcal{P}_{\mathrm{vp}}^2 + \frac{\mathcal{M}_{\mathrm{vp}}}{2}\frac{\mathrm{i}\omega}{\omega_{\mathrm{vp}}}} \right)^{-1}, \qquad \omega_{\mathrm{vp}} = \frac{\phi_{\mathrm{p}}\,\nu}{\mathcal{K}_{0\mathrm{p}}\,\alpha_{\infty\mathrm{p}}}\,, \tag{9}$$

$$\Theta_{\mathrm{p}}(\omega) = \Theta_{0\mathrm{p}} \left(\frac{\mathrm{i}\omega}{\omega_{\mathrm{tp}}} + 1 - \mathcal{P}_{\mathrm{tp}} + \sqrt{\mathcal{P}_{\mathrm{tp}}^2 + \frac{\mathcal{M}_{\mathrm{tp}}}{2}\frac{\mathrm{i}\omega}{\omega_{\mathrm{tp}}}} \right)^{-1}, \qquad \omega_{\mathrm{tp}} = \frac{\phi_{\mathrm{p}}\,\nu_{\mathrm{t}}}{\Theta_{0\mathrm{p}}}\,, \tag{10}$$

where the characteristic (angular) frequencies for viscous ω_{vp} and thermal ω_{tp} effects depend on the kinematic viscosity ν and thermal diffusivity ν_{t} of air, respectively. The imaginary parts of $\mathcal{K}_{\mathrm{p}}$ and Θ_{p} have extremal values around their characteristic frequencies, i.e. close to $f_{\mathrm{vp}} = \frac{\omega_{\mathrm{vp}}}{2\pi}$ and $f_{\mathrm{tp}} = \frac{\omega_{\mathrm{tp}}}{2\pi}$, respectively. The values of these frequencies are listed in Table 2. They were calculated for the three variants of absorber dimensions shown in Table 1, and the air properties $\nu = 1.56 \cdot 10^{-5}\,\mathrm{m}^2/\mathrm{s}$ and $\nu_{\mathrm{t}} = 2.21 \cdot 10^{-5}\,\mathrm{m}^2/\mathrm{s}$ determined during the experimental testing at ambient mean pressure $P_0 = 99650\,\mathrm{Pa}$ and temperature of $23.1\,^{\circ}\mathrm{C}$. The effective compressibility associated with the entire network of annular slits is calculated as

$$\mathcal{C}_{\mathrm{p}}(\omega) = \frac{\phi_{\mathrm{p}}}{P_0} \left(1 - \frac{\gamma - 1}{\gamma}\frac{\Theta_{\mathrm{p}}(\omega)}{\Theta_{0\mathrm{p}}}\frac{\mathrm{i}\omega}{\omega_{\mathrm{tp}}} \right), \tag{11}$$

where $\gamma = 1.4$ is the adiabatic index for air. The effective properties of $\mathcal{C}_{\mathrm{p}}$ and $\mathcal{K}_{\mathrm{p}}$ are sufficient to describe

the acoustics of rigid-frame media with single porosity, e.g. the absorber 3D printed from resin in SLA technology, shown in Figure 1(c,d).

Notice that the scaling functions (9) and (10) of the JCALP model are used to approximate $\mathcal{K}_{\mathrm{p}}(\omega)$ and $\Theta_{\mathrm{p}}(\omega)$ at once for the for entire network of slits. This is a general approach suitable for any pore network. It was applied here for the sake of simplicity and because it gives in fact very accurate results. However, the slits are separated and it is possible and formally more correct to apply the JCALP approximations directly to each of them. Therefore, the scaling functions of the form (9) and (10) can be used to calculate the dynamic viscous $\mathcal{K}_{\mathrm{p}n}(\omega)$ and thermal $\Theta_{\mathrm{p}n}(\omega)$ permeabilities, respectively, separately for each of the three slits Ω_{n}, with $n = 2, 4, 6$. This would require the calculation of the corresponding shape factors using formulae similar to equations (8), as well as characteristic frequencies for each slit. In particular, instead of ω_{vp} and ω_{tp} there are in fact three viscous characteristic frequencies $\omega_{\mathrm{vp}n}$ (for which ω_{vp} is only some average value) and three thermal ones $\omega_{\mathrm{tp}n}$ (for which ω_{tp} is only some average value), respectively. Similarly, the contributing effective compressibilities $\mathcal{C}_{\mathrm{p}n}(\omega)$ are determined separately for each slit Ω_{n}, with $n = 2, 4, 6$, using formulae analogous to equation (11) with the corresponding $\phi_{\mathrm{p}n}$, $\omega_{\mathrm{tp}n}$, $\Theta_{0\mathrm{p}n}$, and $\Theta_{\mathrm{p}n}(\omega)$. Finally, the dynamic viscous permeability and effective compressibility for the entire network of slits are calculated as the sum of the contributions determined for each slit, viz. $\mathcal{K}_{\mathrm{p}}(\omega) = \mathcal{K}_{\mathrm{p}2}(\omega) + \mathcal{K}_{\mathrm{p}4}(\omega) + \mathcal{K}_{\mathrm{p}6}(\omega)$ and $\mathcal{C}_{\mathrm{p}}(\omega) = \mathcal{C}_{\mathrm{p}2}(\omega) + \mathcal{C}_{\mathrm{p}4}(\omega) + \mathcal{C}_{\mathrm{p}6}(\omega)$, respectively. It was verified that the difference between the results obtained with the two approaches discussed above is utterly insignificant, especially as the slits are of comparable width and their respective characteristic frequencies are of similar order.

The parts of the absorber manufactured in BJP technology (see Figure 2) are microporous. The microporosity was found to be open and, moreover, to provide a high contrast of permeability with the designed network of annular slits, ultimately resulting in a double-porosity material with a strong pressure diffusion effect. This phenomenon strongly modifies the effective acoustic compressibility $\mathcal{C}_{\mathrm{db}}$ of the double-porosity BJP absorber compared to that (i.e. $\mathcal{C}_{\mathrm{p}}$) determined for the single-porosity SLA specimen. On the other hand, due to the high permeability contrast between the slits and micropores, the dynamic viscous permeabilities can be assumed identical for both absorbers, i.e. $\mathcal{K}_{\mathrm{db}} \approx \mathcal{K}_{\mathrm{p}}$. The macro-parameters related to the pressure diffusion in the double-porosity BJP absorber are calculated here separately for the cylindrical core Ω_1, and each of the two rings, i.e. Ω_3 and Ω_5, see Figure 1(a). Thus, the relevant volume fractions are

$$\phi_{\mathrm{d}1} = \frac{r_1^2}{R_{\mathrm{t}}^2}\,, \qquad \phi_{\mathrm{d}3} = \frac{r_3^2 - r_2^2}{R_{\mathrm{t}}^2}\,, \qquad \phi_{\mathrm{d}5} = \frac{r_5^2 - r_4^2}{R_{\mathrm{t}}^2}\,, \tag{12}$$

while the static pressure diffusions are calculated as follows (see Appendix A)

$$\mathcal{B}_{0\mathrm{d}1} = \frac{\phi_{\mathrm{d}1}\, r_1^2}{8}\,, \tag{13}$$

$$\mathcal{B}_{0\mathrm{d}3} = \frac{\phi_{\mathrm{d}3}\, r_3^2}{8}\left(1 + (r_2/r_3)^2 + \frac{1 - (r_2/r_3)^2}{\ln(r_2/r_3)}\right), \tag{14}$$

$$\mathcal{B}_{0\mathrm{d}5} = \frac{\phi_{\mathrm{d}5}\, r_5^2}{8}\left(1 + (r_4/r_5)^2 + \frac{1 - (r_4/r_5)^2}{\ln(r_4/r_5)}\right). \tag{15}$$

The associated characteristic lengths are simply equal to the core radius and respective annular widths, viz.

$$\Lambda_{\mathrm{d}1} = r_1\,, \qquad \Lambda_{\mathrm{d}3} = r_3 - r_2\,, \qquad \Lambda_{\mathrm{d}5} = r_5 - r_4\,, \tag{16}$$

while the values of static tortuosities are determined as (see Appendix A): $\alpha_{0\mathrm{d}1} = \frac{4}{3}$, $\alpha_{0\mathrm{d}3} = 1.206$, and $\alpha_{0\mathrm{d}5} = 1.200$. The macro-parameters associated with pressure diffusion and calculated separately for each microporous subdomain of the BJP absorber are listed in Table 3, where the corresponding values calculated for the original, i.e. uncorrected, design are given in parentheses (except for $\alpha_{0\mathrm{d}n}$, which are unchanged). Each of the three sets of these macro-parameters (i.e. successively for Ω_{n} with $n = 1$, 3, and 5) is used to calculate the corresponding shape factors

$$\mathcal{M}_{\mathrm{d}n} = \frac{8\mathcal{B}_{0\mathrm{d}n}}{\phi_{\mathrm{d}n}\,\Lambda_{\mathrm{d}n}^2}\,, \qquad \mathcal{P}_{\mathrm{d}n} = \frac{\mathcal{M}_{\mathrm{d}n}}{4\big(\alpha_{0\mathrm{d}n} - 1\big)}\,. \tag{17}$$

Table 3: Macro-parameters and characteristic frequencies for pressure diffusion in the axisymmetric BJP absorber with double porosity (original design values are given in parentheses).

Domain	n	$\phi_{\mathrm{d}n}$ %	$\mathcal{B}_{0\mathrm{d}n}$ $10^{-8}\,\mathrm{m}^2$	$\Lambda_{\mathrm{d}n}$ mm	$\alpha_{0\mathrm{d}n}$ –	$f_{\mathrm{d}n}$ Hz
Ω_1	1	4.00 (4.28)	4.205 (4.816)	2.9 (3)	1.333	1105 (1033)
Ω_3	3	38.62 (39.95)	109.6 (121.5)	5.8 (6)	1.206	409 (382)
Ω_5	5	35.67 (35.67)	26.78 (26.78)	3.0 (3)	1.200	1548 (1548)

and characteristic frequencies $\omega_{\mathrm{d}n}$, see equation (18) below. Now, the scaling function, analogous to the one known from the JCALP model [19, 20, 21, 22, 25], can be used to determine the corresponding dynamic pressure diffusion functions (for $n = 1, 3, 5$) as follows

$$\mathcal{B}_{\mathrm{d}n}(\omega) = \mathcal{B}_{0\mathrm{d}n}\left(\frac{\mathrm{i}\omega}{\omega_{\mathrm{d}n}} + 1 - \mathcal{P}_{\mathrm{d}n} + \sqrt{\mathcal{P}_{\mathrm{d}n}^2 + \frac{\mathcal{M}_{\mathrm{d}n}}{2}\frac{\mathrm{i}\omega}{\omega_{\mathrm{d}n}}}\right)^{-1}, \qquad \omega_{\mathrm{d}n} = \frac{\phi_{\mathrm{d}n}\,\mathcal{D}_{0\mathrm{m}}}{\mathcal{B}_{0\mathrm{d}n}}, \tag{18}$$

where the (angular) characteristic frequencies $\omega_{\mathrm{d}n}$ depend on the static pressure diffusivity

$$\mathcal{D}_{0\mathrm{m}} = \frac{\mathcal{K}_{0\mathrm{m}}}{\eta\,\mathcal{C}_{0\mathrm{m}}} = \frac{P_0\,\mathcal{K}_{0\mathrm{m}}}{\eta\,\phi_{\mathrm{m}}} \tag{19}$$

of the microporous material [24]. The static pressure diffusivity (19) combines the properties of the microporous network with those of the saturating fluid (air), viz.: the static viscous permeability $\mathcal{K}_{0\mathrm{m}}$ of the microporous material and its static effective compressibility $\mathcal{C}_{0\mathrm{m}} = \phi_{\mathrm{m}}/P_0$ (which is the ratio of the microporosity ϕ_{m} to the ambient mean pressure P_0) with the dynamic viscosity η of air. The air viscosity was assumed as $\eta = 1.83 \cdot 10^{-5}$ Pa·s in the ambient conditions (23.1 °C, $P_0 = 99650$ Pa) found during the acoustic testing of absorbers in the impedance tube, while the inherent properties of the microporous material, i.e. $\phi_{\mathrm{m}} = 42.6\%$ and $\mathcal{K}_{0\mathrm{m}} = 0.57 \cdot 10^{-12}\,\mathrm{m}^2$, were measured directly on specially prepared disc-shaped samples. The microporosity value $\phi_{\mathrm{m}} = 43\%$ was confirmed by inverse identification based on sound absorption measurements of the BJP specimen, however, at the same time the viscous permeability was identified as $\mathcal{K}_{0\mathrm{m}} = 2 \cdot 10^{-12}\,\mathrm{m}^2$ (see the next section).

The three characteristic frequencies $f_{\mathrm{d}n} = \frac{\omega_{\mathrm{d}n}}{2\pi}$ ($n = 1, 3, 5$) for pressure diffusion occurring in the microporous core ($n = 1$), inner ring ($n = 3$) and outer ring ($n = 5$) of the BJP absorber are given in Table 3. The imaginary parts of $\mathcal{B}_{\mathrm{d}n}$ reach extreme values around the respective characteristic frequency $f_{\mathrm{d}n}$, which usually provides a strong pressure diffusion effect over a wide range around this frequency.

In fact, an additional and very effective mechanism for dissipating the energy of acoustic waves by pressure diffusion is due to the phase shift between the average pressure in the micropores and that in the main pores [24] (in the case under study, annular slits). Therefore, the ratio between these two local pressures plays an important role in modelling. For the material under consideration, three complex-valued functions $\mathcal{F}_{\mathrm{d}n}(\omega)$ ($n = 1, 3, 5$), describing this ratio are calculated as

$$\mathcal{F}_{\mathrm{d}n}(\omega) = 1 - \frac{\mathcal{B}_{\mathrm{d}n}(\omega)}{\mathcal{B}_{0\mathrm{d}n}}\frac{\mathrm{i}\omega}{\omega_{\mathrm{d}n}}, \tag{20}$$

i.e. one function is computed for each microporous subdomain: Ω_1, Ω_3, and Ω_5. Their real and imaginary parts are shown in Figure 3. From these graphs, it can be expected that the pressure diffusion is significant, since the functions are substantially complex-valued over wide frequency ranges. The extrema of their imaginary parts are located close to their respective characteristic frequencies $f_{\mathrm{d}n}$. Only at very low frequencies below 100 Hz, where $\mathcal{F}_{\mathrm{d}n} \approx 1$, the pressure diffusion effect is weak or negligible.

The core and both rings of the BJP absorber are made of the same microporous material characterised by the effective compressibility $\mathcal{C}_{\mathrm{m}}(\omega)$. Therefore, the dynamic effective compressibility $\mathcal{C}_{\mathrm{db}}(\omega)$ of the ho-

mogenised medium acoustically equivalent to the double-porosity absorber is calculated as

$$\mathcal{C}_{\mathrm{db}}(\omega) = \mathcal{C}_{\mathrm{p}}(\omega) + \mathcal{C}_{\mathrm{m}}(\omega)\Big(\phi_{\mathrm{d1}}\,\mathcal{F}_{\mathrm{d1}}(\omega) + \phi_{\mathrm{d3}}\,\mathcal{F}_{\mathrm{d3}}(\omega) + \phi_{\mathrm{d5}}\,\mathcal{F}_{\mathrm{d5}}(\omega)\Big). \tag{21}$$

When the pressure diffusion effect is ignored (or very weak), the dynamic effective compressibility (21) reduces to $\mathcal{C}_{\mathrm{pm}}(\omega) = \mathcal{C}_{\mathrm{p}}(\omega) + \phi_{\mathrm{d}}\,\mathcal{C}_{\mathrm{m}}(\omega)$ with $\phi_{\mathrm{d}} = \phi_{\mathrm{d1}} + \phi_{\mathrm{d3}} + \phi_{\mathrm{d5}} = 1 - \phi_{\mathrm{p}}$.

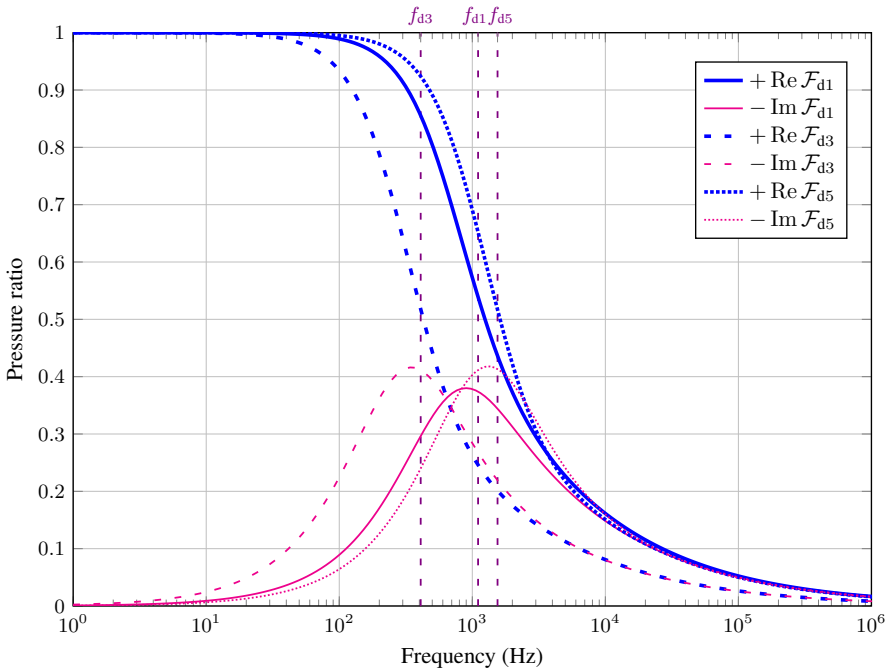

Figure 3: Real and imaginary parts of the pressure ratio functions determined for the microporous core, inner ring, and outer ring of the BJP absorber.

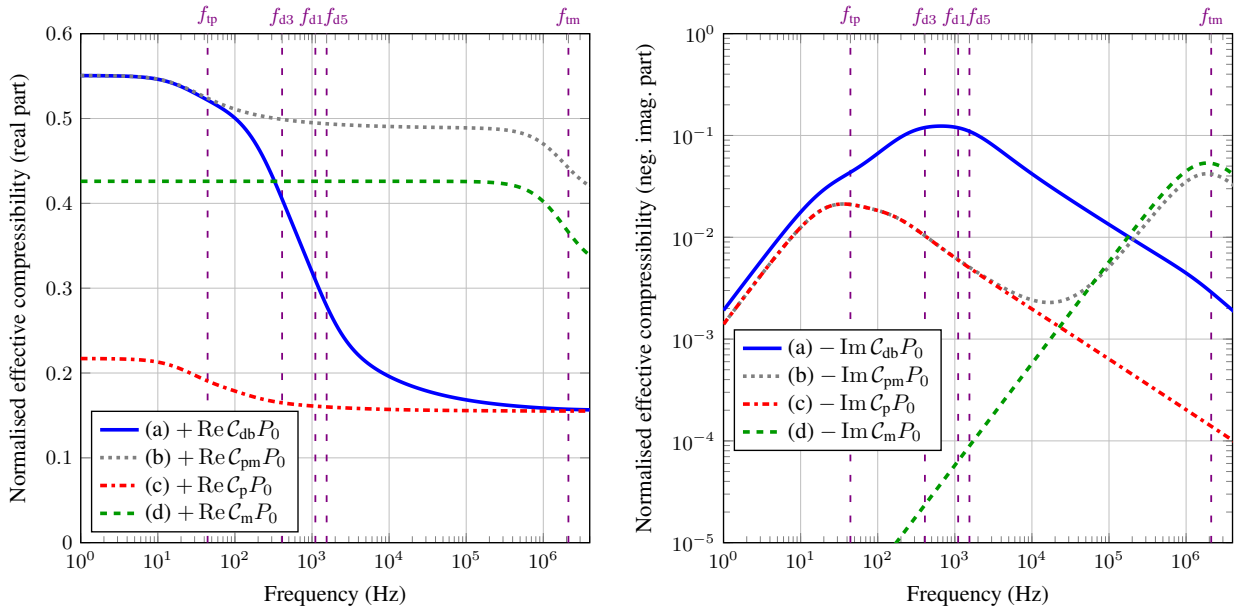

Figure 4: Normalised effective compressibilities determined for: (a) the BJP absorber with double porosity, (b) the BJP absorber but with the pressure diffusion effect ignored, (c) the single-porosity SLA absorber, and (d) the microporous material obtained from gypsum powder.

The real and imaginary parts of the dynamic effective compressibility $\mathcal{C}_{\mathrm{db}}$ (normalised by air compressibility $1/P_0$) determined for the BJP absorber are plotted in Figure 4. It should be observed that the extreme values of the imaginary part form a plateau over a wide frequency range around the three characteristic frequencies $f_{\mathrm{d}n}$ ($n = 1, 3, 5$) related to pressure diffusion occurring in three microporous subdomains. This accounts for a significant increase in the absorption of acoustic wave energy and can be fine tuned by optimising the size of the microporous subdomains. To show the significance of the pressure diffusion effect, the $\mathcal{C}_{\mathrm{db}}P_0$ curves are compared with: (i) the normalised effective compressibility $\mathcal{C}_{\mathrm{pm}}P_0$ calculated for the case where pressure diffusion is ignored, (ii) the normalised effective compressibility $\mathcal{C}_{\mathrm{p}}P_0$ calculated for the single-porosity material with annular slits, and (iii) the normalised compressibility $\mathcal{C}_{\mathrm{m}}P_0$ of the microporous material obtained from gypsum powder. The effective dynamic compressibility for the microporous material $\mathcal{C}_{\mathrm{m}}$ was determined as for a granular medium with known porosity ϕ_{m} and grain size (typical for the gypsum powder used in 3D printing), but in practice it can be replaced with its static counterpart, i.e. $\mathcal{C}_{\mathrm{m}}(\omega) \approx \mathcal{C}_{\mathrm{m}}(0) \equiv \mathcal{C}_{0\mathrm{m}} = \phi_{\mathrm{m}}/P_0$ (see in Figure 4 that $\mathrm{Re}\,\mathcal{C}_{\mathrm{m}}$ is constant and $\mathrm{Im}\,\mathcal{C}_{\mathrm{m}}/\,\mathrm{Re}\,\mathcal{C}_{\mathrm{m}}$ is negligibly small at frequencies below 10 kHz).

4 Sound absorption by axisymmetric absorbers

The dynamic permeability and effective compressibility derived in the previous section for both axisymmetric absorbers permit to calculate their effective acoustic properties, i.e. the effective density ϱ_{e} and speed of sound c_{e}, as follows

$$\varrho_{\mathrm{e}}(\omega) = \frac{\eta}{\mathrm{i}\omega\mathcal{K}_{\mathrm{e}}(\omega)}\,, \qquad c_{\mathrm{e}}(\omega) = \sqrt{\frac{\mathrm{i}\omega\mathcal{K}_{\mathrm{e}}(\omega)}{\eta\,\mathcal{C}_{\mathrm{e}}(\omega)}}\,. \tag{22}$$

In these formulae, $\mathcal{K}_{\mathrm{e}} = \mathcal{K}_{\mathrm{p}}$ and $\mathcal{C}_{\mathrm{e}} = \mathcal{C}_{\mathrm{p}}$ for the single-porosity SLA absorber, while $\mathcal{K}_{\mathrm{e}} = \mathcal{K}_{\mathrm{db}} \approx \mathcal{K}_{\mathrm{p}}$ and $\mathcal{C}_{\mathrm{e}} = \mathcal{C}_{\mathrm{db}}$ for the BJP absorber with double porosity. The dynamic viscosity of air $\eta = 1.83 \cdot 10^{-5}$ Pa·s was determined for the ambient conditions found during the acoustic testing.

The effective properties (22) can be used to determine the acoustic wave propagation in the homogenised domain of the absorber by solving the corresponding Helmholtz problem. This can be done analytically for plane wave propagation with normal incidence to the surface of the cylindrical absorber. From this solution, the surface acoustic impedances Z_{s} of the studied absorbers with a height of $H = 50$ mm are calculated [19] as

$$Z_{\mathrm{s}}(\omega) = -\mathrm{i}\,\varrho_{\mathrm{e}}(\omega)\,c_{\mathrm{e}}(\omega)\cot\big(\omega H/c_{\mathrm{e}}(\omega)\big)\,. \tag{23}$$

Finally, the sound absorption coefficient at normal incidence $\mathcal{A}$ is determined from the acoustic reflection coefficient $\mathcal{R}$ [19] as follows

$$\mathcal{A}(\omega) = 1 - \big|\mathcal{R}(\omega)\big|^2, \qquad \mathcal{R}(\omega) = \frac{Z_{\mathrm{s}}(\omega) - Z_0}{Z_{\mathrm{s}}(\omega) + Z_0}\,, \tag{24}$$

where Z_0 is the characteristic impedance of air. In the ambient conditions found during the acoustic testing $Z_0 = 403.6$ Pa·s/m.

Figure 5 compares sound absorption at normal incidence by the single-porosity SLA absorber and double-porosity BJP absorber, predicted from analytical calculations and measured in the impedance tube [18]. The experimental result for SLA absorber agrees very well with the corresponding analytical prediction (cf. the red curve marked with squares with the orange dotted curve), which proves that the single-porosity model can be used for absorbers 3D printed from photopolymer resins in the SLA technology. In this case, another absorption curve calculated for the uncorrected design with the original annular widths (see the first row of Table 1) is also presented as grey dotted curve in Figure 5, showing only a slight difference at the first absorption peak. Much larger discrepancies between the measurement and the prediction are observed in the case of the absorber with double porosity, especially at frequencies above 2 kHz, cf. the red curve marked with circles with the thick blue curve specified in the graph legend as (BJP) case (a). To some extent, these discrepancies can be attributed to imperfections in the 3D printed absorber, in particular, surface roughness and shape distortions clearly present in the assembled BJP specimen. It has been found, however, that these

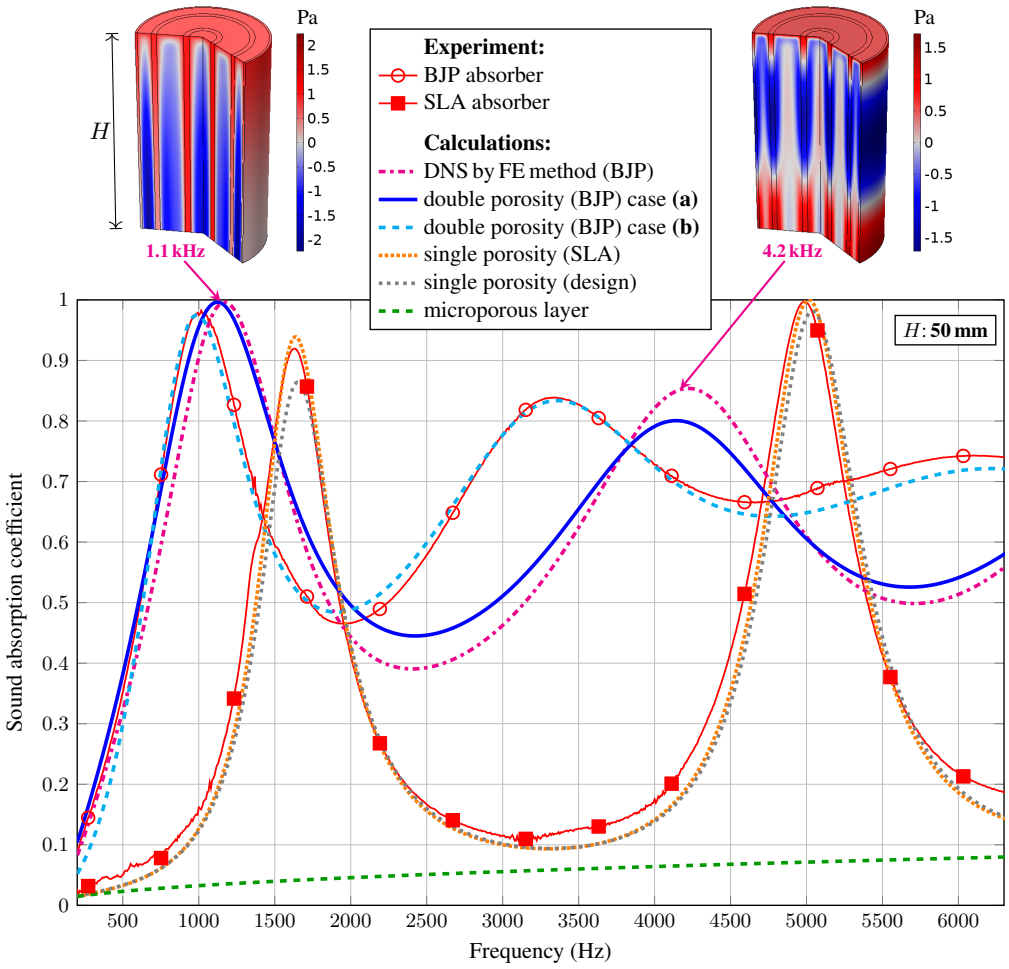

Figure 5: Sound absorption for the 3D printed absorbers with single (SLA) and double (BJP) porosity: measurements vs. predictions. The analytical calculations for the BJP absorber were performed for: (a) directly measured $\mathcal{K}_{0\mathrm{m}} = 0.57 \cdot 10^{-12}\,\mathrm{m}^2$, and (b) inversely identified $\mathcal{K}_{0\mathrm{m}} = 2 \cdot 10^{-12}\,\mathrm{m}^2$.

rather large discrepancies may also result from the incorrectly assumed permeability of the microporous parts of the absorber. Recall that the assumed value $\mathcal{K}_{0\mathrm{m}} = 0.57 \cdot 10^{-12}\,\mathrm{m}^2$ was measured for disc-shaped samples several times thicker than the width of the thickest ring of the absorber. Thicker samples may contain inhomogeneities that reduce permeability, although further research is needed to confirm this. Meanwhile, the value of $\mathcal{K}_{0\mathrm{m}} = 2 \cdot 10^{-12}\,\mathrm{m}^2$ found through inverse identification allowed for a very close matching of the measured and calculated results, cf. the red curve marked with circles with the light blue dashed curve specified in the graph legend as (BJP) case (b). At the same time, the identified microporosity $\phi_{\mathrm{m}} = 43\%$ turned out to be practically the same as the value measured directly. Thus, for acoustic absorbers made in the BJP technology using the suggested 3D printer and a coarse-grained gypsum powder as raw material, the applied modelling which takes into account the double porosity with high contrast of permeability is necessary and at the same time sufficient for correct predictions.

Both absorbers have almost identical networks of annular slits, but their performance differs significantly due to pressure diffusion in the microporous skeleton of the BJP absorber, for which the absorption is almost perfect at its first peak. Moreover, this peak is shifted to a lower frequency around 1 or 1.1 kHz, compared to 1.7 kHz where the first absorption peak of the single-porosity absorber appears. To demonstrate that the increase in absorption is virtually solely due to the effect of double porosity with pressure diffusion, the graph in Figure 5 also presents the extremely poor absorption calculated for a microporous layer with the same thickness $H = 50$ mm as the height of the axisymmetric absorbers.

Figure 5 also shows the results of direct numerical simulation (DNS) carried out for the double-porosity

absorber using the finite element (FE) method. FE mesh depicted in Figure 1(b) has been used for this purpose. The mesh is two-dimensional due to the axial symmetry, and it consists of two material subdomains marked in light blue and orange, respectively; they are: (i) air in the slits and in the top $15\,\mathrm{mm}$ layer adjacent to the absorber, and (ii) the lossy acoustic fluid equivalent to the microporous material of the gypsum skeleton. The later is characterised by the effective density and speed of sound calculated using equations (22) with $\mathcal{K}_\mathrm{e} = \mathcal{K}_\mathrm{m}$ and $\mathcal{C}_\mathrm{e} = \mathcal{C}_\mathrm{m}$, where the dynamic viscous permeability $\mathcal{K}_\mathrm{m}$ and effective compressibility $\mathcal{C}_\mathrm{m}$ of the microporous material can be in practice approximated by their static counterparts, viz. $\mathcal{K}_\mathrm{m}(\omega) \approx \mathcal{K}_\mathrm{m}(0) \equiv \mathcal{K}_\mathrm{0m}$ and $\mathcal{C}_\mathrm{m}(\omega) \approx \mathcal{C}_\mathrm{m}(0) \equiv \mathcal{C}_\mathrm{0m} = \phi_\mathrm{m}/P_0$. The Helmholtz problem for the acoustic pressure variable is solved in each subdomain with the boundary conditions as shown in Figure 1(b), viz.: the axial symmetry at the axis, the rigid wall (i.e. homogeneous Neumann boundary condition) at the bottom and right edges to simulate hard backing and tube walls, and the pressure boundary condition (i.e. Dirichlet condition imposing acoustic pressure of $1\,\mathrm{Pa}$) at the top edge to simulate the effect of incident plane acoustic wave. Now, instead of using equation (23), the numerical surface acoustic impedance Z_s is found at the top boundary (where the wave propagation is lossless) as the ratio of the sound pressure to the normal velocity on that boundary (averaged over the surface, though usually constant, since the boundary is above the absorber where the waves are plane). The sound absorption is again determined using formulae (24) and plotted in Figure 5 with the purple dash-dotted line. This absorption curve is consistent with the corresponding analytical prediction (solid blue line). Discrepancies can be attributed to the fact that the air in the slits is modelled in the DNS as a lossless, inviscid fluid. To illustrate the complex pressure distribution in double-porosity media, the real parts of the acoustic pressure distribution in the BJP absorber found by FE analyses at $1.1\,\mathrm{kHz}$ and $4.2\,\mathrm{kHz}$ are shown above the graph in Figure 5. The phase shift between the pressure in the slits and that in the microporous skeleton, responsible for the increased dissipation of the energy of acoustic waves, is clearly visible.

5 Conclusions

- Double-porosity acoustic absorbers can be easily prototyped by 3D printing structures with designed annular pores – or more complex pore networks – in BJP technology from coarse-grained gypsum powders, using the appropriate amount of binder and other process parameters that result in open microporosity.
- A beneficial high contrast of the permeability between the microporous skeleton, 3D printed in this way, and the main network of designed, (e.g. annular) pores can be easily obtained. As a result, the pressure diffusion effect takes place, which provides an additional mechanism for dissipating the energy of acoustic waves, and thus significantly changes the nature of the sound absorption curves by shifting their peaks to lower frequencies and improving the overall absorption between them.
- Pressure diffusion effect is easily fine-tuned in axisymmetric absorbers by optimising the number and size of the microporous core and rings and the annular slits separating them.
- All this has been confirmed by comparisons of the results of acoustical measurements performed on 3D printed specimens with single and double porosity with the corresponding predictions analytically calculated for the designed axisymmetric absorbers, and verified with direct numerical simulations.
- The discrepancies between the modelling predictions and the experimental results can be attributed to imperfections caused by the manufacturing process, in particular to the surface roughness and shape distortions of the designed annular pores. Another reason may be the uncertainty and inaccuracy in determining the permeability of the microporous structure 3D printed in the BJP technology due to possible inhomogeneities and/or dependence on thickness, which however, requires further research. In particular, the reproducibility of the 3D printed samples with double porosity should be investigated for different powder batches, designed thicknesses, etc.

Acknowledgements

T. G. Zieliński acknowledges the financial support from the project "Sound-absorbing composites: coupled acoustic energy dissipation mechanisms, multiscale modelling and prototyping", financed under Grant Agreement No. 2021/41/B/ST8/04492 by the National Science Centre (NCN), Poland. R. Venegas acknowledges support from the Chilean National Agency for Research and Development (ANID) through FONDECYT Grant No. 1211310.

References

[1] I. Gibson, D. Rosen, and B. Stucker, *Additive Manufacturing Technologies: 3D Printing, Rapid Prototyping, and Direct Digital Manufacturing*, 2nd ed., Springer, New York, 2015.

[2] F. Zhang, L. Zhu, Z. Li, S. Wang, J. Shi, W. Tang, N. Li, and J. Yang, "The recent development of vat photopolymerization: A review," *Additive Manufacturing*, vol. 48, p. 102423, 2021.

[3] A. Mostafaei, A. M. Elliott, J. E. Barnes, F. Li, W. Tan, C. L. Cramer, P. Nandwana, and M. Chmielus, "Binder jet 3D printing—Process parameters, materials, properties, modeling, and challenges," *Progress in Materials Science*, vol. 119, p. 100707, 2021.

[4] T. G. Zieliński, K. C. Opiela, P. Pawłowski, N. Dauchez, T. Boutin, J. Kennedy, D. Trimble, H. Rice, B. Van Damme, G. Hannema, R. Wróbel, S. Kim, S. Ghaffari Mosanenzadeh, N. X. Fang, J. Yang, B. Briere de La Hosseraye, M. C. Hornikx, E. Salze, M.-A. Galland, R. Boonen, A. Carvalho de Sousa, E. Deckers, M. Gaborit, and J.-P. Groby, "Reproducibility of sound-absorbing periodic porous materials using additive manufacturing technologies: Round robin study," *Additive Manufacturing*, vol. 36, p. 101564, 2020.

[5] F. Setaki, M. Tenpierik, M. Turrin, and A. van Timmeren, "Acoustic absorbers by additive manufacturing," *Building and Environment*, vol. 72, pp. 188–200, 2014.

[6] T. G. Zieliński, "Pore-size effects in sound absorbing foams with periodic microstructure: modelling and experimental verification using 3D printed specimens," in *Proceedings of ISMA2016 International Conference on Noise and Vibration Engineering and USD2016 International Conference on Uncertainty in Structural Dynamics*, P. Sas, D. Moens, and A. van de Walle, Eds., 2016, pp. 95–104.

[7] E. R. Fotsing, A. Dubourg, A. Ross, and J. Mardjono, "Acoustic properties of periodic micro-structures obtained by additive manufacturing," *Applied Acoustics*, vol. 148, pp. 322–331, 2019.

[8] K. C. Opiela and T. G. Zieliński, "Microstructural design, manufacturing and modelling of an adaptable porous composite sound absorber," *Composites Part B: Engineering*, vol. 187, p. 107833, 2020.

[9] J. Boulvert, J. Costa-Baptista, T. Cavalieri, M. Perna, E. R. Fotsing, V. Romero-García, G. Gabard, A. Ross, J. Mardjono, and J.-P. Groby, "Acoustic modeling of micro-lattices obtained by additive manufacturing," *Applied Acoustics*, vol. 164, p. 107244, 2020.

[10] H. J. Rice, J. Kennedy, P. Göransson, L. Dowling, and D. Trimble, "Design of a Kelvin cell acoustic metamaterial," *Journal of Sound and Vibration*, vol. 472, p. 115167, 2020.

[11] L. Suárez and M. del Mar Espinosa, "Assessment on the use of additive manufacturing technologies for acoustic applications," *The International Journal of Advanced Manufacturing Technology*, vol. 109, pp. 2691–2705, 2020.

[12] J. Carbajo, J. Molina-Jordá, L. P. Maiorano, and N. X. Fang, "Sound absorption of macro-perforated additively manufactured media," *Applied Acoustics*, vol. 182, p. 108204, 2021.

[13] W. Johnston and B. Sharma, "Additive manufacturing of fibrous sound absorbers," *Additive Manufacturing*, vol. 41, p. 101984, 2021.

[14] J. Boulvert, T. Humbert, V. Romero-García, G. Gabard, E. R. Fotsing, A. Ross, J. Mardjono, and J.-P. Groby, "Perfect, broadband, and sub-wavelength absorption with asymmetric absorbers: Realization for duct acoustics with 3D printed porous resonators," *Journal of Sound and Vibration*, vol. 523, p. 116687, 2022.

[15] R. Venegas and C. Boutin, "Acoustics of permeable heterogeneous materials with local non-equilibrium pressure states," *Journal of Sound and Vibration*, vol. 418, pp. 221–239, 2018.

[16] R. Venegas and C. Boutin, "Enhancing sound attenuation in permeable heterogeneous materials via diffusion processes," *Acta Acustica United With Acustica*, vol. 104, pp. 623–635, 2018.

[17] M. Nori and R. Venegas, "Sound propagation in porous materials with annular pores," *The Journal of the Acoustical Society of America*, vol. 141, no. 6, pp. 4642–4651, 2017.

[18] *ISO 10534-2: Determination of sound absorption coefficient and impedance in impedance tubes*, International Organisation for Standardization, 1998.

[19] J. F. Allard and N. Atalla, *Propagation of Sound in Porous Media: Modeling Sound Absorbing Materials, Second Edition*, John Wiley & Sons, Chichester, 2009.

[20] D. L. Johnson, J. Koplik, and R. Dashen, "Theory of dynamic permeability and tortuosity in fluid-saturated porous media," *Journal of Fluid Mechanics*, vol. 176, pp. 379–402, 1987.

[21] Y. Champoux and J.-F. Allard, "Dynamic tortuosity and bulk modulus in air-saturated porous media," *Journal Applied Physics*, vol. 70, pp. 1975–1979, 1991.

[22] D. Lafarge, P. Lemarinier, J. F. Allard, and V. Tarnow, "Dynamic compressibility of air in porous structures at audible frequencies," *The Journal of the Acoustical Society of America*, vol. 102, pp. 1995–2006, 1997.

[23] C. Boutin, P. Royer, and J. Auriault, "Acoustic absorption of porous surfacing with dual porosity," *International Journal of Solids and Structures*, vol. 35, pp. 4709–4737, 1998.

[24] X. Olny and C. Boutin, "Acoustic wave propagation in double porosity media," *The Journal of the Acoustical Society of America*, vol. 114, no. 1, pp. 73–89, 2003.

[25] S. R. Pride, F. D. Morgan, and A. F. Gangi, "Drag forces of porous-medium acoustics," *Physical Review B*, vol. 47, pp. 4964–4978, 1993.

[26] S. Gasser, F. Paun, and Y. Bréchet, "Absorptive properties of rigid porous media: Application to face centered cubic sphere packing," *The Journal of the Acoustical Society of America*, vol. 117, pp. 2090–2099, 2005.

[27] C. Perrot, F. Chevillotte, and R. Panneton, "Bottom-up approach for microstructure optimization of sound absorbing materials," *The Journal of the Acoustical Society of America*, vol. 124, pp. 940–948, 2008.

[28] T. G. Zieliński, R. Venegas, C. Perrot, M. Červenka, F. Chevillotte, and K. Attenborough, "Benchmarks for microstructure-based modelling of sound absorbing rigid-frame porous media," *Journal of Sound and Vibration*, vol. 483, p. 115441, 2020.

[29] T. G. Zieliński, F. Chevillotte, and E. Deckers, "Sound absorption of plates with micro-slits backed with air cavities: Analytical estimations, numerical calculations and experimental validations," *Applied Acoustics*, vol. 146, pp. 261–279, 2019.

Appendix

A Axisymmetric calculations

A.1 Poisson's equation

It can be demonstrated [17, 29] that for porous media with channels or slits of arbitrary but constant cross-sections and parallel to the flow direction, the Stokes problem degenerates into the Poisson equation. Consequently, the static viscous permeability is equal to the thermal permeability, i.e. $\mathcal{K}_0 = \Theta_0$, and the static viscous tortuosity is the same as the thermal one, i.e. $\alpha_{0\mathrm{v}} = \alpha_{0\mathrm{t}}$. Moreover, such media are, by definition, not tortuous, i.e. with (kinematic) tortuosity $\alpha_\infty = 1$. Their viscous and thermal characteristic lengths are equal to each other and $2\Lambda_\mathrm{v} = 2\Lambda_\mathrm{t}$ is the well-known hydraulic diameter calculated as four times the ratio of the total area of the cross-sections of the slits or channels to their total circumference. Thus, only the Poisson equation has to be solved on the fluid domain to determine the complete set of macro-parameters required by the scaling function. For double-porosity media, a similar Poisson equation must also be solved on the domain of microporous skeleton.

In the axial symmetry case, the only independent variable is the distance from the axisymmetric axis, defined by the radius r, and the Poisson equation becomes an ordinary differential equation of the second-order, viz.

$$\frac{\mathrm{d}^2\theta(r)}{\mathrm{d}r^2} + \frac{1}{r}\frac{\mathrm{d}\theta(r)}{\mathrm{d}r} = -1\,, \tag{25}$$

for which the general solution is

$$\theta(r) = c_1 + c_2 \ln(r/R) - \frac{r^2}{4} \tag{26}$$

where c_1, c_2 are integration constants and $R > 0$ is an arbitrarily chosen radius (e.g. the domain boundary radius is a very convenient choice for R when taking into account the boundary conditions). Particular solutions for circular and annular domains are given in Appendices A.2 and A.3.

As mentioned above, the respective static tortuosities, characteristic lengths, and static permeabilities are identical for viscous and thermal effects, i.e. $\alpha_{0\mathrm{v}} = \alpha_{0\mathrm{t}} = \alpha_0$, $\Lambda_\mathrm{v} = \Lambda_\mathrm{t} = \Lambda$, and $\mathcal{K}_0 = \Theta_0 = \Pi_0$, where α_0, Λ, and Π_0 can be calculated from the analytical formulae derived below for the case of circular and annular domains. Similarly, the static tortuosities, characteristic lengths, and static "permeability" related to pressure diffusion are computed from the same formulae as for the thermal diffusion, i.e. $\alpha_{0\mathrm{d}} = \alpha_0$, $\Lambda_\mathrm{d} = \Lambda$, and $\mathcal{D}_0 = \Pi_0$, but for the respective microporous domains of circular or annular shapes.

A.2 Circular domain

Consider the Poisson problem (25) on an axisymmetric circular domain $\Omega_\mathrm{C} = \{r : 0 \le r \le R\}$ with radius R. Assuming that the solution (26) has to be finite, in particular in the centre of domain, i.e. $|\theta(0)| < \infty$, and also satisfies homogeneous Dirichlet condition on the boundary, i.e. $\theta(R) = 0$, the following result is obtained

$$\theta(r) = \frac{R^2 - r^2}{4} = \frac{R^2}{4}\Big(1 - (r/R)^2\Big). \tag{27}$$

The averaging of $\theta(r)$ and $\theta^2(r)$ over the circular domain Ω_C yields, respectively,

$$\Big\langle \theta(r) \Big\rangle_{\Omega_\mathrm{C}} = \frac{2}{R^2}\int_0^R \theta(r) r \mathrm{d}r = \frac{R^2}{8}\,, \qquad \Big\langle \theta^2(r) \Big\rangle_{\Omega_\mathrm{C}} = \frac{2}{R^2}\int_0^R \theta^2(r) r \mathrm{d}r = \frac{R^4}{48}\,. \tag{28}$$

Let ϕ_{C} be the volume fraction of the circular domain Ω_{C}. The static permeability, characteristic length (i.e. hydraulic radius), and static tortuosity for this domain are

$$\Pi_0 = \phi_{\mathrm{C}} \Big\langle \theta(r) \Big\rangle_{\Omega_{\mathrm{C}}} = \frac{\phi_{\mathrm{C}} R^2}{8}\,, \qquad \Lambda = R\,, \qquad \alpha_0 = \frac{\Big\langle \theta^2(r) \Big\rangle_{\Omega_{\mathrm{C}}}}{\Big\langle \theta(r) \Big\rangle^2_{\Omega_{\mathrm{C}}}} = \frac{4}{3}\,. \tag{29}$$

A.3 Annular domain

Consider the Poisson problem (25) on an axisymmetric annular domain $\Omega_{\mathrm{A}} = \{r : 0 < R_0 \leq r \leq R\}$ with inner boundary radius R_0 and outer boundary radius R, and homogeneous Dirichlet boundary conditions applied on both boundaries, i.e. $\theta(R_0) = 0$ and $\theta(R) = 0$. The solution to such a boundary value problem is

$$\theta(r) = \frac{R^2 - r^2}{4} - \frac{R^2 - R_0^2}{4\ln(R_0/R)} \ln(r/R) = \frac{R^2}{4}\left(1 - (r/R)^2 - \frac{1-\xi^2}{\ln \xi} \ln(r/R)\right), \tag{30}$$

where $\xi = (R_0/R)$. The averaging of $\theta(r)$ and $\theta^2(r)$ over the annular domain Ω_{A} yields, respectively,

$$\begin{aligned} \Big\langle \theta(r) \Big\rangle_{\Omega_{\mathrm{A}}} &= \frac{2}{R^2 - R_0^2} \int_{R_0}^{R} \theta(r) r \mathrm{d}r = \frac{R^2}{8}\left(1 + \xi^2 + \frac{1-\xi^2}{\ln \xi}\right), \\ \Big\langle \theta^2(r) \Big\rangle_{\Omega_{\mathrm{A}}} &= \frac{2}{R^2 - R_0^2} \int_{R_0}^{R} \theta^2(r) r \mathrm{d}r = \frac{R^4}{48}\left(1 + \xi^2 + \xi^4 + \frac{9\left(1-\xi^4\right)}{4\ln \xi} + \frac{3\left(1-\xi^2\right)^2}{2\ln^2 \xi}\right). \end{aligned} \tag{31}$$

Let ϕ_{A} be the volume fraction of the annular domain Ω_{A}. The static permeability, characteristic length (i.e. hydraulic radius), and static tortuosity for this domain are

$$\begin{aligned} \Pi_0 &= \phi_{\mathrm{A}} \Big\langle \theta(r) \Big\rangle_{\Omega_{\mathrm{A}}} = \frac{\phi_{\mathrm{A}} R^2}{8}\left(1 + \xi^2 + \frac{1-\xi^2}{\ln \xi}\right), \qquad \Lambda = R - R_0 = R\,(1-\xi)\,, \\ \alpha_0 &= \frac{\Big\langle \theta^2(r) \Big\rangle_{\Omega_{\mathrm{A}}}}{\Big\langle \theta(r) \Big\rangle^2_{\Omega_{\mathrm{A}}}} = \frac{4}{3} \cdot \frac{1 + \xi^2 + \xi^4 + \frac{9\left(1-\xi^4\right)}{4\ln \xi} + \frac{3\left(1-\xi^2\right)^2}{2\ln^2 \xi}}{\left(1 + \xi^2 + \frac{1-\xi^2}{\ln \xi}\right)^2}\,. \end{aligned} \tag{32}$$

Note that for $\xi \to 0$ the above solution and formulae reduce to the corresponding equations derived in Appendix A.2 for the circular domain.